PHYSICAL REVIEW B **93**, 115150 (2016)

Bona fide interaction-driven topological phase transition in correlated symmetry-protected topological states

Yuan-Yao He,[1] Han-Qing Wu,[1] Yi-Zhuang You,[2] Cenke Xu,[2] Zi Yang Meng,[3] and Zhong-Yi Lu[1]
[1]*Department of Physics, Renmin University of China, Beijing 100872, China*
[2]*Department of Physics, University of California, Santa Barbara, California 93106, USA*
[3]*Beijing National Laboratory for Condensed Matter Physics, and Institute of Physics, Chinese Academy of Sciences, Beijing 100190, China*

(Received 2 October 2015; revised manuscript received 12 March 2016; published 31 March 2016)

It is expected that the interplay between nontrivial band topology and strong electron correlation will lead to very rich physics. Thus a controlled study of the competition between topology and correlation is of great interest. Here, employing large-scale quantum Monte Carlo simulations, we provide a concrete example of the Kane-Mele-Hubbard model on an AA-stacking bilayer honeycomb lattice with interlayer antiferromagnetic interaction. Our simulation identified several different phases: a quantum spin Hall insulator (QSH), an xy-plane antiferromagnetic Mott insulator, and an interlayer dimer-singlet insulator. Most importantly, a bona fide topological phase transition between the QSH and the dimer-singlet insulators, purely driven by the interlayer antiferromagnetic interaction, is found. At the transition, the spin and charge gap of the system close while the single-particle excitations remain gapped, which means that this transition has no mean-field analog and it can be viewed as a transition between bosonic symmetry-protected topological (SPT) states. At one special point, this transition is described by a $(2+1)d$ $O(4)$ nonlinear sigma model with exact $SO(4)$ symmetry and a topological term at exactly $\Theta = \pi$. The relevance of this work towards more general interacting SPT states is discussed.

DOI: 10.1103/PhysRevB.93.115150

I. INTRODUCTION

The interplay between nontrivial band topology and strong electron interaction is expected to lead to a plethora of new physical phenomena in strongly correlated systems. Many exotic phenomena of interacting topological insulators (TIs) have been predicted/discovered, such as topological Kondo insulators [1–3], fractionalized TIs [4,5], interaction-reduced classification of TIs [6–16], and interaction-driven anomalous topological order at the boundary of TIs [12,17–22]. Besides fermionic systems, it was also proposed that bosonic systems can also form exotic states that are similar to fermionic TIs [23,24], which are generally called the symmetry-protected topological (SPT) states. Unlike their fermionic counterparts, bosonic SPT states can only exist in strongly interacting boson systems, and the interaction must be carefully designed to avoid the ordinary superfluid and Mott insulator phases. These studies have tremendously broadened our understanding of quantum disordered states of matter and revealed the fundamental role topology plays in condensed matter systems.

Quantum phase transitions between different stable quantum disordered phases is another important subject, and in general it can be very different from the standard Ginzburg-Landau (GL) phase transition paradigm. For example, one expects that a phase transition between a $(2+1)d$ topologically ordered state (Z_2 spin liquid [25]) and a conventionally ordered phase (superfluid) is beyond the GL paradigm, and that the Landau order parameter will acquire an enormous anomalous dimension. This phenomenon is confirmed by unbiased quantum Monte Carlo simulations [26,27]. In the noninteracting limit, the quantum critical point between two different topological insulators is usually described by a gapless Dirac/Majorana fermion, but the role of strong interaction at this transition has not been fully explored, although we understand that in some particular cases interaction can gap out this quantum critical point and lead to a continuous curve connecting the two sides of the phase diagram [6,7]. Quantum phase transitions between bosonic SPT states were even less studied, and it was pointed out that most generally two bosonic SPT states can be separated by an intermediate phase [28,29].

With this in mind, it will be of great interest to investigate a concrete example where in a strongly correlated fermionic SPT setup there is a purely interaction-driven phase transition between a topological insulator and a quantum disordered phase. Such a bona fide interaction-driven topological phase transition will have no mean-field (noninteracting) correspondence and provide the precious example of a controlled study of the interplay between nontrivial band topology and strong electron interaction. And this is what we will focus on in this paper.

Here, we provide a concrete simple interacting fermion model that is studied by large-scale unbiased quantum Monte Carlo (QMC) simulations. The results of this investigation provide us with the following desired phenomenon: a bona fide interaction-driven quantum phase transition between a topological insulator and a strongly interacting Mott insulator (a quantum disordered phase). We find that this quantum critical point is fundamentally different from the TI-to-trivial quantum phase transition in the free-fermion limit, in the sense that the fermions never close their gap at the transition, but emergent collective bosonic degrees of freedom become critical. Thus we can view this transition as a transition between a bosonic SPT state and a trivial bosonic Mott insulator. And we demonstrate that at one special point, this transition is described by a $(2+1)d$ $O(4)$ nonlinear sigma model with exact $SO(4)$ symmetry and a topological term at exactly $\Theta = \pi$. Moreover, we also employ the strange correlator proposed by Ref. [30] and tested in Refs. [31–34] to diagnose the topological nature of the interaction-driven quantum phase transition between a topological insulator and the strongly interacting Mott insulator.

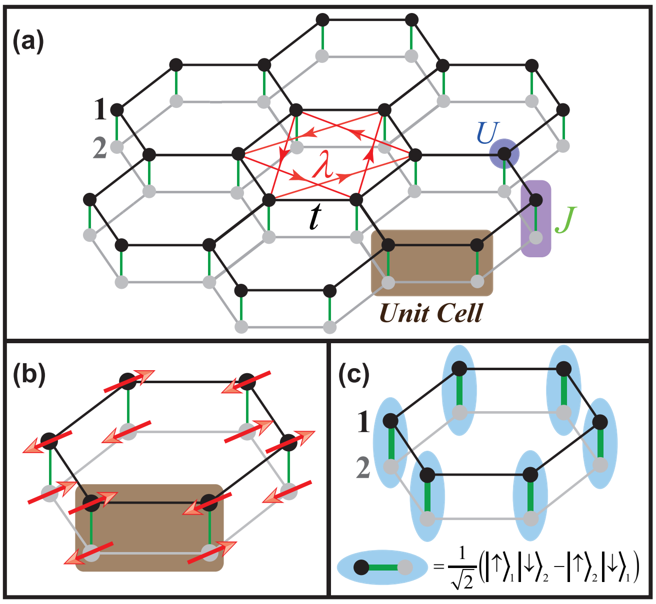

FIG. 1. (a) Illustration of AA-stacked honeycomb lattice and bilayer KMH model with interlayer antiferromagnetic exchange interaction. The four-site unit cell is presented as the shaded rectangle. The gray and black lines indicate the nearest-neighbor hopping t on layers 1 and 2, respectively. The spin-orbital coupling term λ, for one spin flavor, is shown by the red lines and arrows with $\nu_{ij} = +1$. The on-site Coulomb repulsion and interlayer AFM coupling are represented by the shaded circle and rectangle, respectively. (b) Illustration of the xy-AFM Mott insulator phase. (c) Illustration of the interlayer dimer-singlet phase. Shaded ellipses are the interlayer spin singlets.

II. MODEL AND NUMERICAL METHOD

A. AA-stacked bilayer KMH model with interlayer AFM coupling

In this work, we employ large-scale QMC simulations to investigate the AA-stacked bilayer Kane-Mele-Hubbard (KMH) model with interlayer antiferromagnetic (AFM) coupling; the Hamiltonian is given by $\hat{H} = \hat{H}_{TB} + \hat{H}_U + \hat{H}_J$ as

$$\begin{aligned}\hat{H} = &-t\sum_{\xi\langle i,j\rangle,\alpha}(c^\dagger_{\xi i\alpha}c_{\xi j\alpha}+c^\dagger_{\xi j\alpha}c_{\xi i\alpha})\\ &+i\lambda\sum_{\xi\langle\langle i,j\rangle\rangle,\alpha\beta}\nu_{ij}\left(c^\dagger_{\xi i\alpha}\sigma^z_{\alpha\beta}c_{\xi j\beta}-c^\dagger_{\xi j\beta}\sigma^z_{\beta\alpha}c_{\xi i\alpha}\right)\\ &+\frac{U}{2}\sum_{\xi i}(n_{\xi i\uparrow}+n_{\xi i\downarrow}-1)^2\\ &+\frac{J}{8}\sum_i[(D_{1i,2i}-D^\dagger_{1i,2i})^2-(D_{1i,2i}+D^\dagger_{1i,2i})^2],\end{aligned} \tag{1}$$

with $D_{1i,2i} = \sum_\sigma c^\dagger_{1i\sigma}c_{2i\sigma}$. α, β denote the spin species ↑ and ↓ and $\xi = 1,2$ stand for the layer index in the AA-stacked bilayer system, as shown in Fig. 1. H_{TB} describes the tight-binding part of the Hamiltonian, including the nearest-neighbor hopping and the spin-orbit coupling [35,36] terms, and the factor $\nu_{ij} = -\nu_{ji} = \pm 1$ depends on the orientation of the two nearest-neighbor bonds that the electron traverses in going from site j to i, as shown in Fig. 1(a). The $\sigma^z_{\alpha\beta}$ in the spin-orbit coupling term furthermore distinguishes the ↑ and ↓ spin states with the opposite next-nearest-neighbor hopping amplitude. Throughout this work, we take t as the unit of energy. The second term H_U describes the on-site Coulomb repulsion between electrons, and $n_{\xi i} = \sum_\sigma n_{\xi i\sigma}$. The electron filling is fixed at half filled, i.e., one electron per site on average. The third term H_J stands for the interlayer antiferromagnetic spin interaction. As explained in detail in Appendix A, it is a faithful approximation of the full Heisenberg interaction $J\sum_i \mathbf{S}_{1i}\cdot\mathbf{S}_{2i}$.

The Kane-Mele (KM) model preserves time-reversal symmetry Z_2^T and its ground state is a quantum spin Hall insulator with counterpropagating edge states [35,36]. On the AA-stacked bilayer honeycomb lattice, the ground state of the KM model is still a quantum spin Hall (QSH) insulator but with two sets of counterpropagating edge modes. As for the symmetry, the model Hamiltonian in Eq. (1) has charge $U(1)\times U(1)$ symmetry, which corresponds to charge conservation on each individual layer. The $SU(2)$ spin-rotational symmetry is broken down to $U(1)$ by the spin-orbit coupling term; the residual $U(1)$ spin symmetry corresponds to the spin rotation in the xy plane. Therefore, most generally the total symmetry of the AA-stacked bilayer model is $U(1)_{\text{spin}}\times[U(1)\times U(1)]_{\text{charge}}\rtimes Z_2^T$, which results in a $\mathbb{Z}$ classification. This is because in the noninteracting limit we can define a Chern number for spin-up and spin-down electrons separately, and time-reversal symmetry guarantees that these two Chern numbers must be equal. Thus eventually the whole system is characterized by one Chern number, which can take arbitrary integer values. When including interaction terms, we found that at the limit of $U = 0$, Eq. (1) has a much higher $SO(4)$ symmetry, which we will analyze in detail in Sec. III B.

With interactions, the KMH model on the monolayer honeycomb lattice has been studied by the Hartree-Fock mean-field theory [37], cluster (dynamic) mean-field theory [38–40], as well as determinantal QMC simulations [31,41–48]. For the bilayer model in Eq. (1), at the $U = J = 0$ limit, the system is a QSH insulator with spin Chern number $C_s = (C_\uparrow - C_\downarrow)/2 = 2$, where $C_\uparrow = +2$ and $C_\downarrow = -2$ are the Chern numbers for spin-up and spin-down parts. In the presence of finite interactions, i.e., the U-J phase diagram, one can expect that in the large-U limit, the bilayer system will be driven from the QSH state into an xy-plane AFM ordered (xy-AFM) Mott insulator phase, through a continuous phase transition, similar to the KMH model on a monolayer honeycomb lattice [31,37–48], and that the phase transition should belong to the $(2+1)d$ XY universality class [43,48]. At the large-J limit, the bilayer system should enter the interlayer dimer-singlet phase with spin singlets formed on the interlayer bonds due to strong antiferromagnetic coupling J. In the $J\to\infty$ limit, the interlayer dimer-singlet phase is a product state of the interlayer singlets in which all the symmetries are preserved [49]. Combining the spin-orbit coupling term λ, on-site Coulomb repulsion U, and interlayer coupling J, one can expect very interesting competition occurring among the QSH, xy-AFM, and interlayer dimer-singlet phases, and it is the quantum phase transitions between these phases (some of which are of exotic topological nature) that we engaged in great effort to unravel in this paper with unbiased large-scale QMC simulations.

B. Projector quantum Monte Carlo method

The projector QMC (PQMC) method is the zero-temperature version of the determinantal QMC algorithm [50]. The PQMC method obtains the ground-state expectation values of physical quantities by carrying out an imaginary-time evolution of some trial wave function, which is not orthogonal to the true many-body ground state. The ground-state expectation value of physical observable is calculated as follows,

$$\langle \hat{O} \rangle = \lim_{\Theta \to +\infty} \frac{\langle \psi_T | e^{-\Theta \hat{H}/2} \hat{O} e^{-\Theta \hat{H}/2} | \psi_T \rangle}{\langle \psi_T | e^{-\Theta \hat{H}} | \psi_T \rangle}, \tag{2}$$

where $|\psi_T\rangle$ is the trial wave function and Θ is the projection parameter. In all the simulations, to ensure that the algorithm arrives at the truly converged ground state of finite-size systems, we choose $\Theta = 60/t, \Delta\tau = 0.05/t$, in which $\Delta\tau$ is the finite imaginary-time step applied in the Trotter decomposition of partition function. During the simulations, we adopt the Hubbard-Stratonovich (HS) transformation with four-component Ising fields to decouple the interaction terms [51]. Due to the fact that the two terms in the H_J interaction do not commute, the systematic error for all physical observables is at the order of $\mathcal{O}(\Delta\tau)$ (Trotter error). During the simulation, we make sure that the value of $\Delta\tau$ is small enough and the QMC sampling of physical observables is large enough that the results are numerically exact within well-characterized statistical errors. We have simulated different linear system size $L = 3,6,9,12$ ($L = 15$ for strange correlator), with $N = L^2$ as the number of unit cells to extrapolate physical observables to the thermodynamic limit.

To determine the phase diagram for the bilayer model in Eq. (1), we first measure static physical quantities, such as the expectation values of energy densities (both total and each individual term in the Hamiltonian), double occupancy, and spin-spin correlation function. The xy-plane AFM order is expected to have ordering vector $\mathbf{\Gamma} = (0,0)$ [31,40–49]; the transverse magnetic structure factor at the $\mathbf{\Gamma}$ point is measured as

$$S^{xy}(\mathbf{\Gamma}) = \frac{1}{4N} \sum_{ij\gamma} \langle S^x_{i\gamma} S^x_{j\gamma} + S^y_{i\gamma} S^y_{j\gamma} \rangle, \tag{3}$$

where $i,j = 1,2,\ldots,N$ run over all unit cells and $\gamma = 1,2,3,4$ stands for the four sublattices inside a unit cell. The staggered magnetic moment m_S can be evaluated as $m_S = \sqrt{S^{xy}(\mathbf{\Gamma})/N}$.

Next, to have the dynamical information of the system, such as the excitation gaps in single- and two-particle channels, we need to measure the imaginary-time single-particle Green's function,

$$G(\mathbf{k},\tau) = \frac{1}{4N} \sum_{ij\gamma\sigma} e^{i\mathbf{k}\cdot(\mathbf{R}_i - \mathbf{R}_j)} \langle c^\dagger_{i\gamma\sigma}(\tau) c_{j\gamma\sigma} \rangle, \tag{4}$$

where γ is again the sublattice index and σ is the electron spin, the imaginary-time spin-spin correlation function at the $\mathbf{\Gamma}$ point,

$$S^{xy}(\mathbf{\Gamma},\tau) = \frac{1}{4N} \sum_{ij\gamma} \langle S^x_{i\gamma}(\tau) S^x_{j\gamma} + S^y_{i\gamma}(\tau) S^y_{j\gamma} \rangle, \tag{5}$$

and the imaginary-time interlayer pair-pair correlation function in the charge channel,

$$P(\mathbf{\Gamma},\tau) = \frac{1}{2N} \sum_{ij\delta} \langle \Delta^\dagger_{i\delta}(\tau) \Delta_{j\delta} + \Delta^\dagger_{j\delta}(\tau) \Delta_{i\delta} \rangle, \tag{6}$$

where $\Delta_{i\delta} = \frac{1}{\sqrt{2}}(c_{1,i,\uparrow,\delta} c_{2,i,\downarrow,\delta} - c_{1,i,\downarrow,\delta} c_{2,i,\uparrow,\delta})$ is the interlayer Cooper pair operator, which is defined on the two interlayer bonds $\delta = 1,2$ of each unit cell i. At the $\tau \to \infty$ limit, we access the asymptotic behavior $G(\mathbf{k},\tau) \propto e^{-\Delta_{sp}(\mathbf{k})\tau}$, $S^{xy}(\mathbf{\Gamma},\tau) \propto e^{-\Delta_S \tau}$, and $P(\mathbf{\Gamma},\tau) \propto e^{-\Delta_C \tau}$ in which $\Delta_{sp}(\mathbf{k})$ is the single-particle excitation gap and Δ_S, Δ_C are the two-particle excitation gaps in the spin and charge channels for the interacting system [52]. In our bilayer system, the minimum value of the single-particle gap appears either at $\mathbf{k} = \mathbf{K}$ or $\mathbf{k} = \mathbf{M}$ depending on the parameters U and J, and we measure the spin and charge gaps at the $\mathbf{\Gamma}$ point as it is the ordered wave vector for the gapless Goldstone modes.

To diagnose the topological nature of the quantum phase transition, we employ the recently developed strange correlator method [30–34]. In the single-particle and two-particle (spin) channels, the correlation functions are constructed as

$$C^\sigma_{\mathbf{k}AB} = \frac{\langle \Omega | c^\dagger_{\mathbf{k}A\sigma} c_{\mathbf{k}B\sigma} | \Psi \rangle}{\langle \Omega | \Psi \rangle}, \quad S^\pm_{\mathbf{k}AA} = \frac{\langle \Omega | S^+_{\mathbf{k}A} S^-_{\mathbf{k}A} | \Psi \rangle}{\langle \Omega | \Psi \rangle}, \tag{7}$$

where $c^\dagger_{\mathbf{k}A\sigma} = \frac{1}{L} \sum_{\xi,i} e^{i\mathbf{k}\cdot\mathbf{R}_{\xi i}} c^\dagger_{\xi i,A,\sigma}$ and $S^+_{\mathbf{k}A} = \frac{1}{L} \sum_{\xi,i} e^{i\mathbf{k}\cdot\mathbf{R}_{\xi i}} S^+_{\xi i,A}$ (integer i as unit cell index), with $\mathbf{k}$ inside the Brillouin zone (BZ) region, A, B the sublattices in a unit cell in one layer, and ξ the layer index, as shown in Fig. 1. The basic idea of the strange correlator is that, on the left-hand side of the correlation function, the wave function $|\Omega\rangle$ is a trivial band insulator (with spin Chern number $C_s = 0$); on the right-hand side of the correlation function, the projection operator $e^{-\Theta\hat{H}}$ guarantees that $|\Psi\rangle = e^{-\Theta\hat{H}}|\Psi_T\rangle$ is the many-body ground state wave function of the bilayer KMH Hamiltonian at certain J and U. If $|\Psi\rangle$ is a topologically nontrivial QSH state, i.e., there exist gapless edge modes at the spatial boundary of $|\Psi\rangle$, then after a space-time rotation, $C^\sigma_{\mathbf{k}AB}$ will develop a singularity at a certain symmetric momentum point $\mathbf{k}_s$: $C_\mathbf{k} \sim 1/|\mathbf{k} - \mathbf{k}_s|^\alpha$, with $\alpha = 1$ for a noninteracting system, $\alpha < 1$ otherwise. Based on the effective Lorentz invariant description of topological insulators [53], the 2D strange correlator $C^\sigma_{\mathbf{k}AB}$ should behave very similarly to the $(1+1)d$ correlation functions at the boundary, endowed with a Luttinger liquid description in the presence of interaction. If $|\Psi\rangle$ is on the other hand a topologically trivial insulator, then the divergence in $C^\sigma_{\mathbf{k}AB}$ is no longer present as there are no single-particle edge modes on the boundary of $|\Psi\rangle$. What is more, the spin strange correlator $S^\pm_{\mathbf{k}AA}$ also has different behaviors, depending on whether the gapless two-particle edge modes are present or not. For the QSH insulator, $S^\pm_{\Gamma AA}$ should possess a diverging behavior faster than $\sim \ln L$ (the case in noninteracting systems) with increasing system size L, while it should saturate to finite value (slower than $\sim \ln L$ behavior) in a topologically trivial insulator. Thus, one can readily detect the topological phase transition in the system by monitoring the behavior of $C^{\sigma}_{\mathbf{k}AB}$ and $S^{\pm}_{\Gamma AA}$. The strange correlation has been successfully applied in the QMC investigation of the topological phase transitions in the monolayer KMH model; readers are referred to Ref. [31] for more details on its physical meaning and technical implementation.

III. NUMERICAL RESULTS AND DISCUSSIONS

A. Phase diagram

The U-J phase diagram for $\lambda = 0.2t, 0.3t$ is shown in Fig. 2, and this is one of the main results of the paper. QSH, xy-AFM, and interlayer dimer-singlet phases are found from QMC simulations. Since there is only a net shift in the phase boundaries between the $\lambda = 0.2t$ and $0.3t$ cases, we will focus on the detailed results for the $\lambda = 0.2t$ case in the following. The orange dotted line in Fig. 2 denotes the $J = 2U$ path which is studied in Ref. [49]; we note that with more careful finite-size scaling in our work, we found that it actually goes through an intermediate AFM region.

Three featuring observations about this phase diagram are in order. First of all, at small U ($U < 0.5t$ for $\lambda = 0.2t$) there is a direct phase transition from the QSH insulator to interlayer dimer-singlet insulator (see details in Appendix D). Notice that since neither the QSH nor the dimer-singlet phase has symmetry breaking, all the symmetries (such spin-rotation, charge-conservation, time-reversal, and lattice symmetries) in the model Hamiltonian Eq. (1) are preserved across this phase transition, rendering it a bona fide topological phase transition driven purely by the interlayer antiferromagnetic interaction J. This is a very unique case and very different from the transitions in (interacting) topological insulators that have been studied before [31,37–48,54], where the transitions are either driven by hopping parameters at free-fermion level [40,45,47,48,54], or after the transition the symmetry that protects the nontrivial band topology has been destroyed by interactions [31,37–48,54]. The nature of this exotic transition will be further discussed in the next section.

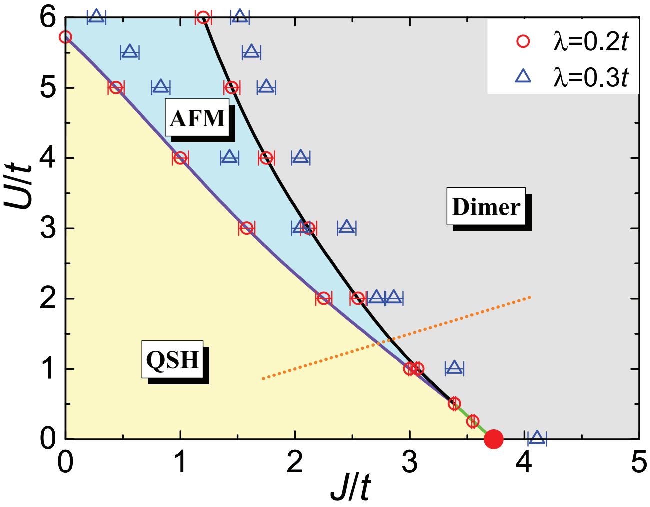

FIG. 2. U-J phase diagram for the AA-stacked bilayer KMH model with interlayer antiferromagnetic coupling. Shown here are the phase diagram for $\lambda = 0.2t$ and $\lambda = 0.3t$ cases. Solid lines (violet, green, and black) are the phase boundaries for the $\lambda = 0.2t$ case. The red solid dot at $(J_c, U = 0)$ and red open dots at $U = 0.25$ and 0.5 and the green line going through them highlight the interaction-driven topological phase transition between QSH and the dimer-singlet insulator phase. The orange dotted line highlights the $J = 2U$ path which is studied in Ref. [49]; it actually goes through a small AFM region.

Second, the region of the xy-AFM phase is greatly extended by an interesting collaboration between the on-site Coulomb repulsion U and the interlayer AFM coupling J. At $J = 0$, for $\lambda = 0.2t$, the QSH to xy-AFM phase transition occurs at $U \approx 5.6(2)t$ [31], but as J increases, the phase boundary between QSH and xy-AFM moves towards smaller U, which means J and U both prefer the AFM state, until J dominates over U, after which the dimer-singlet phase takes over. The same phenomenon is also observed for the $\lambda = 0.3t$ case.

Third, for the direct phase transition from the QSH phase to the interlayer dimer-singlet phase, we have observed signatures of continuous phase transitions. This can be seen from the interlayer spin-spin correlation function per bond, shown in Fig. 3(a) for an $L = 6$ system with $\lambda = 0.2t$ (data with larger system sizes are shown in Appendix D). For various U values, as a function of J, the spin-spin correlation function changes from 0 to $-3/4$, with the latter signifying the formation of spin-singlet on every interlayer bond. Moreover, according to the Hellmann-Feynman theorem, the spin-spin correlation function per bond is the first-order derivative of the total energy density over J. Combining the results of $\langle \boldsymbol{S}_{1i} \cdot \boldsymbol{S}_{2i} \rangle$ presented in Fig. 3(a) and in Appendix D, the continuous changing of the first-order derivative of the total energy density, with increasing J, suggests that the topological phase transition from the QSH to the dimer-singlet insulator phase is continuous (at least for $U = 0$).

To further elaborate upon this point, Figs. 3(b) and 3(c) show the first-order derivatives of expectation values of $\langle H_J \rangle$ per bond and $\langle H_U \rangle$ per site, over the parameter J. The peaks in Fig. 3(b) indicate the QSH to dimer-singlet ($U = 0$) and xy-AFM to dimer-singlet (when $U \geqslant 2t$) phase transitions. The peaks in Fig. 3(c) indicate not only the same transitions in Fig. 3(b) at large J and small U, but more interestingly, also the QSH to xy-AFM phase transitions at small J and large U (for $U \geqslant 3t$), as there are two peaks in the curves for $U = 3t, 4t, 5t$. The finite-size effects in the energy density derivatives are small; we only observe a slight shift of the phase boundaries for $L = 9, 12$ systems, compared with those for the $L = 6$ system shown here. In the next section, we will present the finite-size scaling of the QMC results of the magnetic order parameter as well as the single-particle and spin excitation gaps across the topological phase transition between QSH and dimer-singlet. As we will see, the results hence obtained are consistent with those in Fig. 2 and Fig. 3 in this section.

B. Topological phase transition

1. Excitation gaps

As mentioned in the preceding section (Sec. III A), one of the most exciting features in the phase diagram (Fig. 2) is the exotic topological phase transition purely

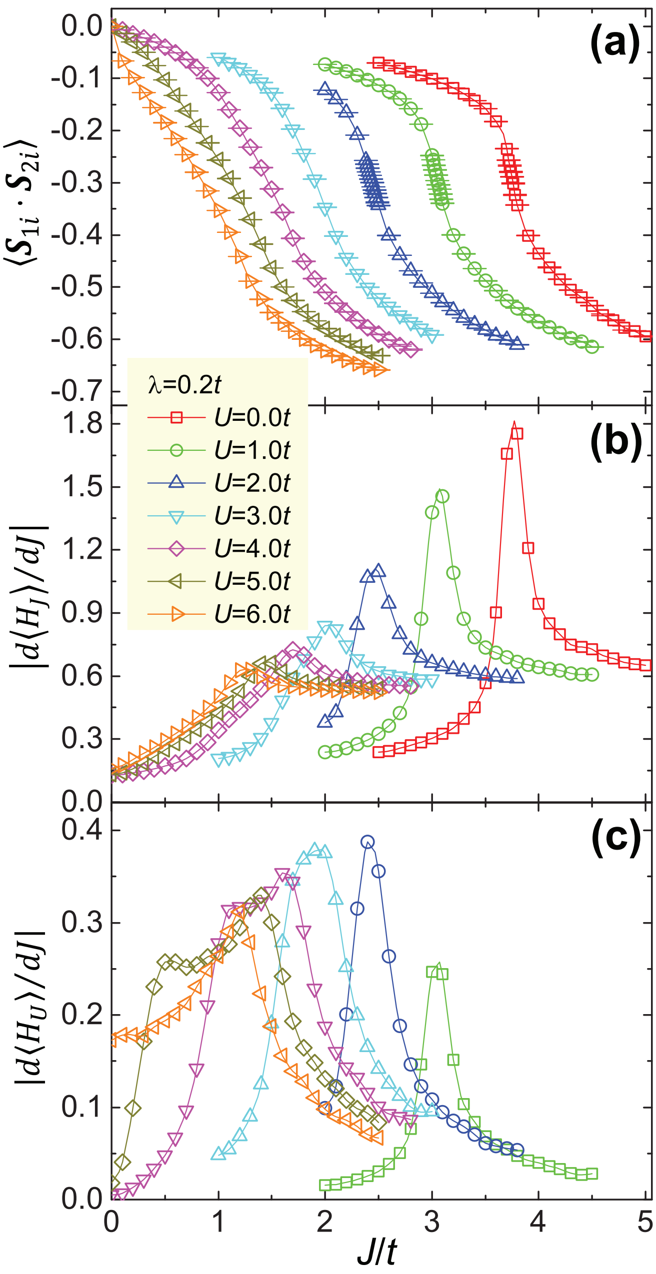

FIG. 3. (a) The interlayer spin-spin correlation function for the $L = 6, \lambda = 0.2t$ system with various U values, as a function of J. The continuous variation of this correlation function indicates that the topological phase transition from QSH to dimer-singlet is a continuous one. At large J, the correlation saturates at $-3/4$ which signifies the formation of interlayer dimer singlets. (b) First-order derivative of $\langle H_J\rangle$ per bond over J for $L = 6, \lambda = 0.2t$. The peak in every curve explicitly indicates phase transition from QSH insulator (or xy-AFM) phase to interlayer dimer-singlet phase. (c) First-order derivative of $\langle H_U\rangle$ per site over J. The peaks in these curves indicate all three possible phase transitions: QSH to dimer-singlet, QSH to xy-AFM, and xy-AFM to dimer-singlet transitions. For $U < 2t$, the peak in $d\langle H_U\rangle/dJ$ corresponds to the QSH to dimer-singlet transition; for $U > 3t$, the two independent peaks as a function of J correspond to the QSH to xy-AFM transition at small J and xy-AFM to dimer-singlet transition at large J.

driven by the interlayer antiferromagnetic interaction J, between the QSH and dimer-singlet phases.

In a free-fermion system, topological phase transitions between SPT states are driven by tight-binding parameters. The single-particle excitation gap will close to zero and reopen continuously at the transition, as long as the symmetries protecting the topologically nontrivial phase are still preserved. However, the topological phase transitions in interacting systems seem to be much more complicated. Of course, they can still be driven by some tight-binding hopping parameter in the model Hamiltonian, such as the third-nearest-neighbor hopping [40,45,47,48], dimerized nearest-neighbor hopping [46–48], Rashba spin-orbit coupling [54], and Kekulé distortion [55] in the monolayer KMH model. In these cases, the single-particle gap closes and reopens at the topological phase transition, just as in their noninteracting counterparts. But, they can furthermore be driven purely by interactions, such as on-site Coulomb repulsion in the monolayer KMH model [31,37,38,41–44,48], interlayer AFM exchange coupling in the AA-stacked bilayer KMH model [49], and the more complicated form of interaction in the interacting Bernevig-Hughes-Zhang model [55].

For interaction-driven topological phase transitions, the on-site Coulomb repulsion in the monolayer KMH model drives the QSH phase into an antiferromagnetically ordered phase with broken time-reversal and spin-rotational symmetries. Precisely speaking, this is still not the topological phase transition we are after in this paper: what we found here is a purely interaction-driven topological phase transition without any symmetry breaking on either side of the transition. Examples of this type of phase transition have been discussed in 1-dimensional [56] and 2-dimensional [49] interacting systems. In Ref. [49], the single-particle gap remains gapped at the transition and it is the spin excitation gap and Cooper pair gap that close and reopen. This implies that in the low-energy limit such topological phase transition only involves bosonic degrees of freedom, allowing the fermionic excitations to be integrated out from the field theory [49].

Following Ref. [49], we perform a detailed study on the topological phase transition between QSH and dimer-singlet phases in the phase diagram of Fig. 2. To characterize this phase transition, we measured the single-particle gap, two-particle spin and charge gaps, as well as the strange correlator [30–34] in the QMC simulations.

The results of single-particle and spin gaps with increasing J are shown in Fig. 4 for $\lambda = 0.2t, U = 0$ in $L = 3,6,9,12$ bilayer systems. The raw data of the single-particle Green's function and dynamic spin-spin correlation function are shown in Appendix B; the data are of very good quality, upon which we extracted the excitation gaps reliably. At $U = 0$, the topological phase transition point is at $J_c \simeq 3.7t$–$3.8t$ in the phase diagram in Fig. 2. As shown in Fig. 4(a), the single-particle gap only exhibits a very gentle dip around the topological phase transition point, which suggests that the single-particle gap of the system remains open as a function of J. In contrast, we observe in Fig. 4(b) that the spin gap decreases rapidly in the vicinity of J_c as a function of system size L. The inset of Fig. 4(b) shows the gap values

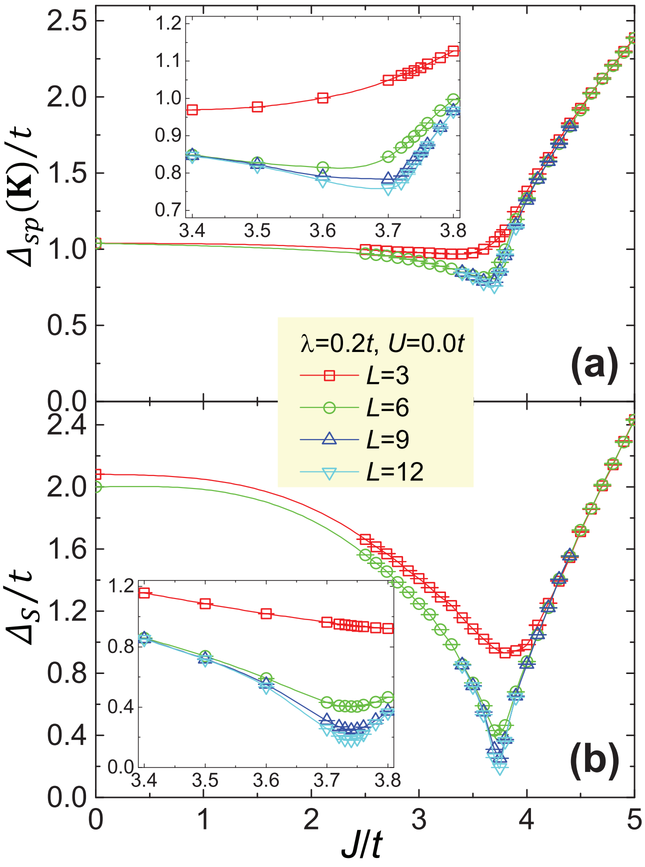

FIG. 4. (a) Single-particle gap $\Delta_{sp}(\mathbf{K})$ of $\lambda = 0.2t, U = 0$ as a function of J. The inset shows the $\Delta_{sp}(\mathbf{K})$ in $J \in [3.4t, 3.8t]$ region. We have checked that $\mathbf{K}$ point is indeed the minimum of single-particle gap in the whole BZ. As a function of J, the single-particle gap only shows a gentle dip near the topological phase transition. (b) Spin gap Δ_S of $\lambda = 0.2t, U = 0$ with increasing J. The inset is the spin gaps in the $J \in [3.4t, 3.8t]$ region. The spin gap drops very fast and closes at the topological phase transition point $J_c = 3.73(1)t$.

in the region $J \simeq 3.4t$–$3.8t$. Within an even smaller region of $J \in [3.7t, 3.8t]$, we extrapolate the spin gap values for $L = 3,6,9,12$ systems in $1/L$ to estimate the spin gap in the thermodynamic limit, which is shown in Fig. 5. The main panel and inset of Fig. 5 deliver a clear message that the spin gap closing point is around $J_c = 3.73(1)t$. Furthermore, at $U = 0$ as a function of J, we do not find a stepping of xy-AFM order by finite-size extrapolation of the transverse magnetic structure factor (see details in Appendix D). At $J = 3.8t$, the spin gap values for the $L = 9$ system and $L = 12$ are almost the same, indicating that the thermodynamic limit is already reached and the spin excitations are well gapped here (spin-spin correlation in real space is exponentially short-ranged). After the topological phase transition, the bilayer system enters the interlayer dimer insulator phase, which is schematically shown in Fig. 1(c).

Combining the results for single-particle and spin gaps, we find that the topological phase transition driven by interlayer AFM coupling in our bilayer system is fundamentally different from that controlled by the hopping parameters, with and without interactions [31,37–48,54].

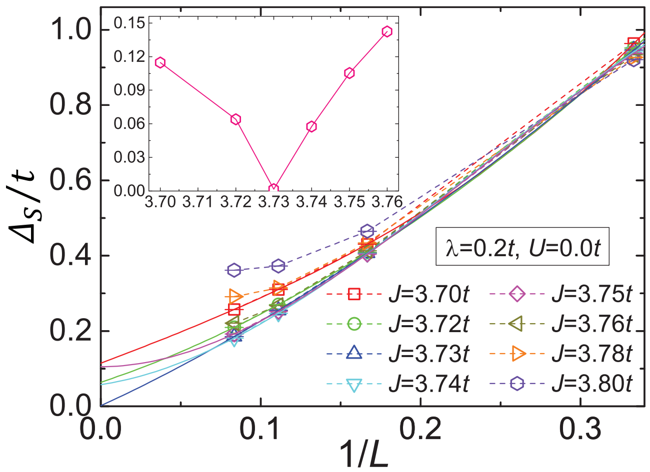

FIG. 5. Spin gap in the $J \in [3.7t, 3.8t]$ region for $\lambda = 0.2t, U = 0$ with $L = 3,6,9,12$ and the extrapolation by third-order polynomial. The inset shows the extrapolated spin gap as a function of J.

Also, at $U = 0$, we have observed that the charge gap Δ_C and spin gap Δ_S are numerically identical (with difference only up to $0.001t$). There is actually a deep theoretical reason for the equality between these two-particle gaps: it is due to an exact $SO(4)$ symmetry at $U = 0$ (see Appendix C), which rotates the xy-AFM (spin) fluctuation $\boldsymbol{N}_i = \frac{1}{2}(-1)^{i+\xi-1} c_{\xi i}^{\dagger} \boldsymbol{\sigma} c_{\xi i}$ and the pairing (charge) fluctuation $\Delta_i = c_{1i} i \sigma^y c_{2i}$ like an $O(4)$ vector:

$$\boldsymbol{n}_i = \left(N_i^x, \operatorname{Im}\Delta_i, \operatorname{Re}\Delta_i, N_i^y\right). \tag{8}$$

Therefore both the spin and the charge excitation gaps close identically at the transition point. To better understand the $SO(4)$ symmetry, we may define two fermion doublets $f_{i\sigma}$ $(\sigma = \uparrow,\downarrow)$:

$$f_{i\uparrow} = (c_{1i\uparrow}\$ - 1)^i c_{2i\uparrow}^{\dagger}), \quad f_{i\downarrow} = \begin{pmatrix} (-1)^i c_{1i\downarrow} \\ c_{2i\downarrow}^{\dagger} \end{pmatrix}. \tag{9}$$

Then the $O(4)$ vector can be written as

$$\boldsymbol{n}_i = \frac{1}{2} f_{i\uparrow}^{\dagger}(\tau^0, -i\tau^1, -i\tau^2, -i\tau^3) f_{i\downarrow} + \text{H.c.}, \tag{10}$$

where $\tau^{0,1,2,3}$ are the Pauli matrices acting on the f-fermion doublets. The $SO(4)$ group is naturally factorized to $SU(2)_{\uparrow} \times SU(2)_{\downarrow}$ as right and left isoclinic rotations, under which the fermion transforms as $f_{i\sigma}^{\dagger} \mapsto f_{i\sigma}^{\dagger} U_{\sigma}$ with $U_{\sigma} \in SU(2)_{\sigma}$ for both $\sigma = \uparrow,\downarrow$. The model Hamiltonian in Eq. (1) at $U = 0$ can be written in terms of the $SU(2)_{\uparrow} \times SU(2)_{\downarrow}$ singlets as

$$\hat{H} = \sum_{i,j,\sigma} \chi_{\sigma}(f_{i\sigma}^{\dagger} t_{ij} f_{j\sigma} + \text{H.c.}) - \frac{J}{4} \sum_{i} (\hat{P}_i^{\dagger} \hat{P}_i + \hat{P}_i \hat{P}_i^{\dagger}), \tag{11}$$

with

$$\hat{P}_i = \frac{1}{2}(-1)^i \sum_{\sigma} f_{i\sigma}^{\dagger} i\tau^2 (f_{i\sigma}^{\dagger})^{\mathrm{T}}, \tag{12}$$

where we have $\chi_{\sigma} = (-1)^{\sigma}$, and $t_{ij} = t$ for hoppings on the nearest-neighbor bonds and $t_{ij} = i\lambda$ for spin-orbit coupling on the next-nearest-neighbor bonds. Under arbitrary $SU(2)$ rotation of the $f_{i\sigma}^{\dagger}$ operator as $f_{i\sigma}^{\dagger} \mapsto f_{i\sigma}^{\dagger} U_{\sigma}$, the $\hat{P}_i$ operator in Eq. (12) is invariant since we have $f_{i\sigma}^{\dagger} i\tau^2 (f_{i\sigma}^{\dagger})^{\mathrm{T}} \mapsto f_{i\sigma}^{\dagger} U_\sigma i\tau^2 U_\sigma^{\mathrm{T}} (f_{i\sigma}^{\dagger})^{\mathrm{T}}$, and the equality $U_\sigma i\tau^2 U_\sigma^{\mathrm{T}} = i\tau^2$ for 2×2 $SU(2)$ matrix U_σ. Besides, the hopping term $f_{i\sigma}^{\dagger} t_{ij} f_{j\sigma}$ is explicitly invariant under the $SU(2)_\sigma$ rotation of U_σ. Combining them, the Hamiltonian in Eq. (12) has independent $SU(2)_\uparrow$ and $SU(2)_\downarrow$ symmetries for spin up and down channels, respectively. Thus, the $SO(4) \simeq SU(2)_\uparrow \times SU(2)_\downarrow$ symmetry for the bilayer model in Eq. (1) under the $U = 0$ condition, which can be expressed in Eq. (11), is explicit.

Physically, the $SO(4)$ symmetry rotates the four components of $\boldsymbol{n}_i$ defined in Eq. (8) to one another. As a result, the xy-AFM order should be exactly degenerate with the interlayer spin-singlet s-wave superconducting order under the $U = 0$ condition due to the $SO(4)$ symmetry, which also indicates the identical excitation gaps corresponding to these two orders, i.e., spin gap and charge gap.

2. *Theoretical understanding*

In our phase diagram, the fermionic single-particle gap never closes with finite λ, while the two-particle, collective, bosonic modes (spin and charge gaps) both close at the QSH-to-dimer-singlet phase transition; this means that at low energy this model can be well approximated by a bosonic model. Indeed, Ref. [57] demonstrated that many bosonic SPT states can be constructed from fermionic topological insulators/superconductors by confining the fermionic degrees of freedom. In our case, we propose that the bosonic sector of our phase diagram, at $U = 0$, can be described by the following nonlinear sigma model (NLSM) field theory [49]:

$$S = \int d^2x d\tau \, \frac{1}{g}(\partial_\mu \boldsymbol{n})^2 + \frac{i\Theta}{\Omega_3}\epsilon_{abcd} n^a \partial_x n^b \partial_y n^c \partial_\tau n^d, \qquad (13)$$

where $\Omega_3 = 2\pi^2$ is the volume of a three-dimensional sphere with unit radius. We will focus on the phase with large g, namely the vector $\boldsymbol{n}$ is disordered. Equation (13) is exactly the same field theory introduced by Refs. [58,59] to describe $2d$ bosonic SPT states, and the physical meaning of the four-component vector field $\boldsymbol{n}$ was given in Eq. (8). As we show explicitly in Appendix C, the model Eq. (1) at $U = 0$ has exactly $SO(4)$ symmetry; thus we do not need to turn on any anisotropic term to Eq. (13). When we move away from the point $U = 0$, an anisotropy needs to be turned on to split the degeneracy between (n_1,n_4) and (n_2,n_3).

The phase diagram and renormalization group flow of the $(1+1)d$ analog of Eq. (13) were calculated explicitly in Refs. [60–62], and it was demonstrated that the entire phase $0 \leqslant \Theta < \pi$ is controlled by the trivial fixed point $\Theta = 0$, while the entire phase $\pi < \Theta \leqslant 2\pi$ will flow to the fixed point $\Theta = 2\pi$. The phase diagram of Eq. (13) was studied in Ref. [63], and again in the disordered phases (phases with large g) $\Theta = \pi$ is the quantum phase transition between the two phases with $0 \leqslant \Theta < \pi$ and $\pi < \Theta \leqslant 2\pi$; the stable fixed point $\Theta = 2\pi$ describes a bosonic SPT state in $(2+1)d$ [59].

The physical meaning of the fixed point $\Theta = 2\pi$ becomes explicit when we create a vortex of Δ, i.e., the vortex of (n_2,n_3); then this vortex will acquire spin-1 due to the Θ term at $\Theta = 2\pi$, which is consistent with two copies of quantum spin Hall insulator with S^z conservation. Also, at the fixed point $\Theta = 2\pi$, the boundary of Eq. (13) is a $(1+1)d$ $O(4)$ NLSM with a Wess-Zumino-Witten term at level 1 [59,63], whose $SO(4)$ symmetry factorizes into $SU(2)_L \times SU(2)_R$ [$SU(2)$ symmetries for left and right moving modes respectively], where $SU(2)_L$ and $SU(2)_R$ precisely correspond to $SU(2)_\uparrow$ and $SU(2)_\downarrow$ introduced in the previous subsection. Thus the field theory Eq. (13) does match with the all the desired physics of our lattice model. In a later paper by some of us [64], we demonstrate that the boundary state of our lattice model will be driven into a purely bosonic conformal field theory, in the sense that all the fermionic modes are gapped by interaction, but bosonic modes are gapless. And the remaining gapless bosonic modes at the boundary are precisely described by the boundary states of Eq. (13).

In Eq. (13) $\Theta = \pi$ is the quantum phase transition between the SPT and trivial phases, and in our phase diagram $\Theta = \pi$ corresponds to the direct QSH-to-dimer-singlet phase transition. Thus our lattice model actually provides a way to simulate the topological field theory Eq. (13) in QMC without the sign problem.

3. *Strange correlator*

Let us now turn to understanding the topological phase transition from QSH to dimer-singlet phases from the perspective of edge states. At $U = 0$, in the QSH phase with $J < J_c$, there exist two pairs of gapless edge modes on the boundary of the bilayer KMH system, i.e., the spin Chern number $C_s = 2$. When $J > J_c$, the system is the dimer-singlet state; it is a topologically trivial product state hence the edge states are no longer present; i.e., spin Chern number $C_s = 0$. Therefore, the change of the topological nature from QSH to dimer-singlet can be seen from the presence/absence of the gapless edge states.

In the QMC simulations, one can explicitly probe the spatial edge by applying the open boundary condition (OBC), but in interacting systems, OBC usually has very strong finite-size dependence. Moreover, to be able to see the edge mode, one further needs to analytically continue the imaginary-time correlation functions to have the spectra in real frequency, but it is well known that analytical continuation usually generates ambiguous results to the fine features of the spectra. Hence, to avoid such difficulties, recently there has been a new diagnosis dubbed the strange correlator, which has been proposed/tested successfully in probing the edge states from static, bulk wave functions with the periodic boundary condition [30–34].

As explained in the Sec. II B, whether the gapless edge modes are present in the bilayer system or not can be signified by the divergence of the single-particle and spin strange correlator, which are shown in Fig. 6 for $\lambda = 0.2t, U = 0$. From the single-particle strange correlator results in Fig. 6(a), for $J = 3t$ $(J < J_c)$, $|C_{\mathbf{k}AB}^{\uparrow}|$ of the bilayer KHM mode is diverging at the $\mathbf{M}$ point; correspondingly, $1/|C_{\mathbf{k}AB}^{\uparrow}|$ vanishes in a power law (the exponent α is almost 1) to zero. The data point of $1/|C_{\mathbf{k}AB}^{\uparrow}|$ exactly at $\mathbf{k} = \mathbf{M}$ is a finite-size effect due to the implementation of the strange correlator in QMC and has been explained thoroughly in Ref. [31]. But when $J = 4t$ $(J > J_c)$, the divergence of $C_{\mathbf{k}AB}^{\uparrow}$ is removed; hence the $1/|C_{\mathbf{k}AB}^{\uparrow}|$ is no longer vanishing at the $\mathbf{M}$ point, resembling

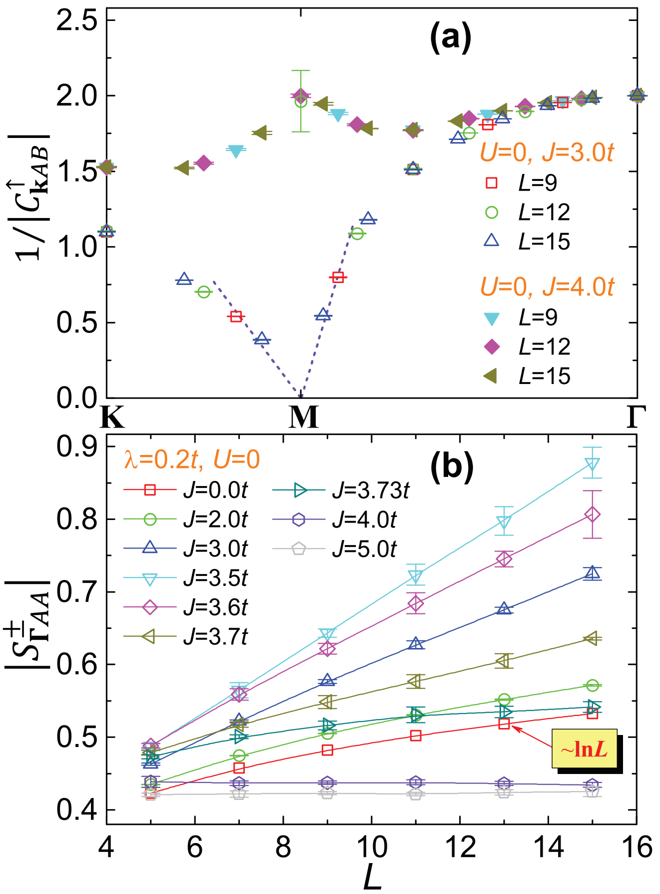

FIG. 6. (a) The inverse amplitude of single-particle strange correlator $1/|C^{\uparrow}_{\mathbf{k}AB}|$ along the high-symmetry path for various $J = 3.0t,4.0t$. (b) The spin strange correlator $S^{\pm}_{\mathbf{k}AA}$ at various J values as a function of linear system size L.

the single-particle edge modes in QSH being gapped out due to the interlayer antiferromagnetic interaction J. As for the spin strange correlator shown in Fig. 6(b), $S^{\pm}_{\mathbf{k}AA}$ diverges with increasing L at $J < J_c$, which is faster than the ln L behavior at the noninteracting limit $J = 0$. These results indicate the existence of gapless, spin (bosonic) edge modes [64]. On the contrary, $S^{\pm}_{\mathbf{k}AA}$ simply saturate to finite values when $J > J_c$, suggesting the absence of gapless edge modes. Combining the results of the strange correlator in both single-particle and two-particle channels, the QSH phase ($J < J_c$) in the bilayer model has gapless edge modes (bosonic), while they are absent in the dimer-singlet insulator phase, highlighting the topological phase transition.

C. *xy*-AFM order

The xy-AFM order in the phase diagram Fig. 2 corresponds to the ordered phase $g < g_c$ in Eq. (13), with an extra anisotropy term that favors (n_1,n_2) over (n_3,n_4). In the phase diagram of Fig. 2, one finds that the region of the xy-AFM phase is greatly extended by an interesting collaboration between the on-site Coulomb repulsion U and the interlayer AFM coupling J. Intuitively, the U term favors the xy-AFM state, while the J term favors the dimer-singlet state. With increasing U, the QSH to xy-AFM and xy-AFM to dimer-singlet phase transition points all move towards smaller J. This can be understood as follows: the xy-AFM phase is triggered by the intralayer antiferromagnetic coupling $J_{\text{intra}} \propto t^2/U$, the dimer-singlet phase is triggered by the interlayer J, their phase transition is determined by the ratio J/J_{intra}, and since we get a smaller J_{intra} for larger U, the critical J for the phase transition to dimer-singlet is therefore reduced.

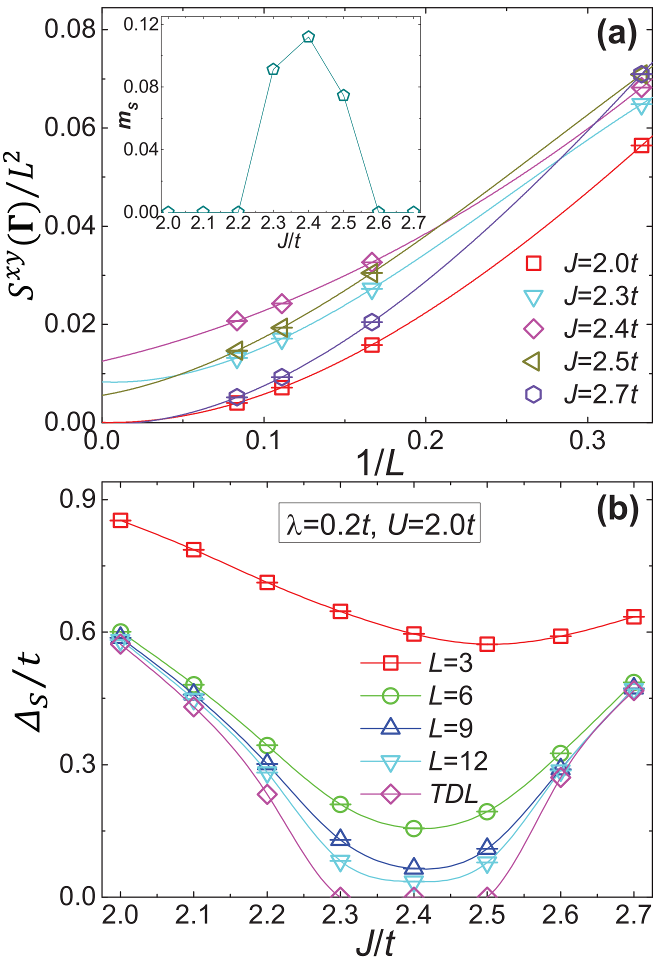

FIG. 7. (a) Finite-size extrapolation of the transverse magnetic structure factor for $L = 3,6,9,12$ systems; the fits are third-order polynomial in $1/L$. The parameters are $\lambda = 0.2t, U = 2t$, and $J \in [2.0t,2.7t]$. Inset shows the extrapolated staggered magnetic moment m_S as a function of J. (b) The spin gap for $L = 3,6,9,12$ systems and its extrapolated thermodynamic limit (TDL) values for the same parameter set.

Let us be more quantitative about the phase boundary. For the monolayer KMH model with $\lambda = 0.2t$, the system enters the xy-AFM phase at $U_c = 5.6(2)t$ [31]. In the presence of interlayer J, QMC results reveal that the xy-AFM phase can be well established even at $U \sim 2t$. As shown in Fig. 7(a), for the magnetic structure factor for $L = 3,6,9,12$ systems and their extrapolation to the thermodynamic limit in $J \in [2.0t,2.7t]$, the extrapolated $S^{xy}(\mathbf{\Gamma})/N$ takes nonzero values for $J = 2.3t,2.4t,2.5t$ [see the inset of Fig. 7(a)]. To further confirm the long-range magnetic order, we have also measured the spin gap and the results are shown in Fig. 7(b). The extrapolated spin gaps at $J = 2.3t,2.4t,2.5t$ are zero and correspond to

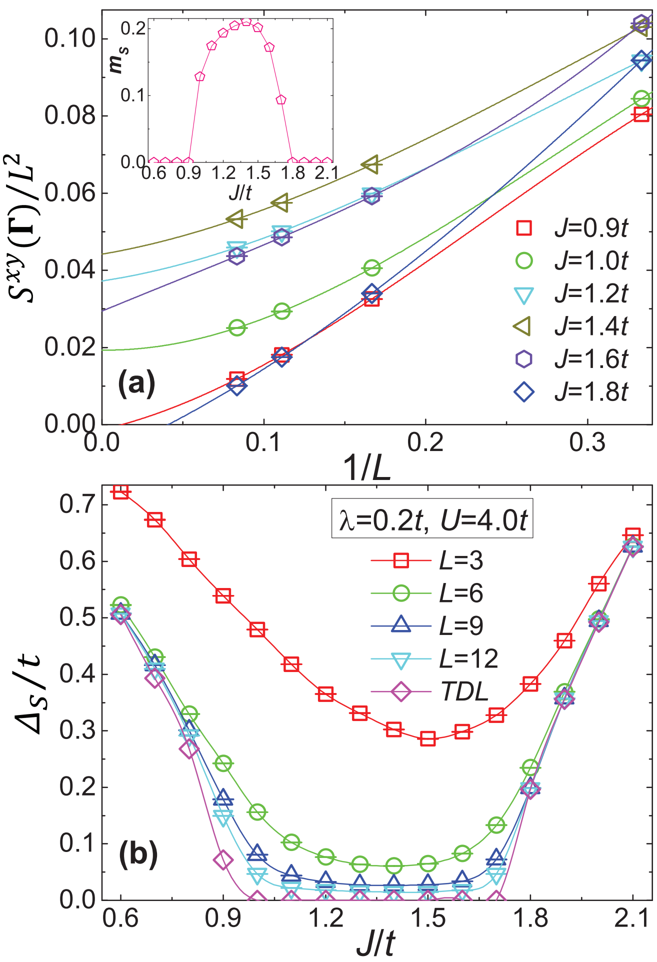

FIG. 8. (a) Finite-size extrapolation of the transverse magnetic structure factor for $L = 3,6,9,12$ systems; the fits are third-order polynomial in $1/L$. The parameter sets are $\lambda = 0.2t, U = 4t$, and $J \in [0.6t, 2.1t]$. Inset shows the extrapolated staggered magnetic moment m_S as a function of J. (b) The spin gap for $L = 3,6,9,12$ systems and its extrapolated thermodynamic limit (TDL) values for the same parameter set.

the Goldstone mode associated with the xy-AFM long-range order. Combining the data in Figs. 7(a) and 7(b), it is very convincing that the long-range xy-plane magnetic order already appears at $U \sim 2t$, almost 3 times smaller than that of the $J = 0$ case.

When the on-site Coulomb repulsion is further increased to $U = 4t$, at $\lambda = 0.2t$ and $J \in [0.6t, 2.1t]$, there are two phase transitions (QSH to xy-AFM and xy-AFM to dimer-singlet) as J increases. These can be detected by measuring the magnetic structure factor and the spin gap as well; the results are shown in Fig. 8. Figure 8(a) shows that the system is in the xy-AFM phase in $J \in [1.0t, 1.7t]$ by finite-size extrapolation. The spin gap result in Fig. 8(b) is quite consistent with it, as the spin excitations are gapless in the thermodynamic limit in $J \in [1.0t, 1.7t]$. When $J \leqslant 1.0t$, the system is inside the QSH insulator where the spin excitations are gapped, and when $J \geqslant 1.7t$, the system is inside the dimer-singlet phase where the spin excitations are gapped as well.

IV. SUMMARY AND OUTLOOK

In this work, we have found a bona fide interaction-driven quantum phase transition between a topological insulator and a strongly interacting Mott insulator (dimer-singlet). This quantum critical point is fundamentally different from the TI-to-trivial quantum phase transition in the noninteracting limit, in the sense that the fermions never close their gap at the transition; instead, emergent collective bosonic degrees of freedom become critical. We also employ the strange correlator proposed/tested in Ref. [30–34] to diagnose the topological nature of the quantum phase transitions.

In principle the exotic topological phase transition that we found in this paper can be generalized to all higher dimensions. What we need to find is a higher-dimensional fermionic topological insulator/superconductor that can be mapped to a bosonic SPT state after confining the fermionic degrees of freedom; then in principle the similar type of SPT-trivial phase transition with gapless boson modes but no gapless fermion mode can be found in these cases. A construction of these models in higher dimensions was discussed in Ref. [57].

Although we have identified the field theory that describes this interaction-driven direct TI-to-trivial quantum phase transition in Eq. (13), we do not yet have a controlled analytical calculation for the universality class of this transition. It seems the ordinary calculation techniques such as $1/N$ or ϵ expansion both fail here, because Eq. (13) is defined solely for the $(2+1)d$ and $O(4)$ vector. How we should compare the critical scaling behavior of the spin gap Δ_S measured in Fig. 5 to theoretical calculations based on Eq. (13) is an interesting open question, which we will leave to future study.

ACKNOWLEDGMENTS

We acknowledge T. Yoshida, Z. Wang, K. Sun, N. Kawakami, X. Dai, and F. Assaad for valuable discussions. The numerical calculations were carried out at the Physical Laboratory of High Performance Computing in Renmin University of China, the Center for Quantum Simulation Sciences in the Institute of Physics, Chinese Academy of Sciences, the National Supercomputer Center in Tianjin on the platform Tianhe-1A, as well as the National Supercomputer Center in GuangZhou on the platform Tianhe-2A. H.Q.W., Y.Y.H., and Z.Y.L. acknowledge support from the National Natural Science Foundation of China (NSFC Grant Nos. 91421304 and 11474356). C.X. and Y.Z.Y. are supported by the David and Lucile Packard Foundation and NSF Grant No. DMR-1151208. Z.Y.M. is supported by the NSFC (Grants No. 11421092 and No. 11574359) and the National Thousand-Young-Talents Program of China and acknowledges the hospitality of the KITP at the University of California, Santa Barbara, where part of this work was completed.

APPENDIX A: APPROXIMATE HEISENBERG INTERACTION

In Sec. II A, we mention that the interlayer antiferromagnetic interaction in our Hamiltonian is a faithful approximation of the full antiferromagnetic Heisenberg interaction. Here we elaborate more upon this point.

The interlayer interaction term H_J in Eq. (1) can be written as summation of the following term on all inter-layer bonds,

$$\hat{Q}_i = \tfrac{1}{8}[(D_{1i,2i} - D^{\dagger}_{1i,2i})^2 - (D_{1i,2i} + D^{\dagger}_{1i,2i})^2]. \quad \text{(A1)}$$

There is an operator identity relating $\hat{Q}_i$ to full Heisenberg exchange coupling [51]; it reads

$$\mathbf{S}_{1i} \cdot \mathbf{S}_{2i} = \hat{Q}_i - \tfrac{1}{4}[(\hat{n}_{1,i} - 1)(\hat{n}_{2,i} - 1) - 1], \quad \text{(A2)}$$

so the difference between $\hat{Q}_i$ and $\mathbf{S}_{1i} \cdot \mathbf{S}_{2i}$ is at the part $[(\hat{n}_{1,i} - 1)(\hat{n}_{2,i} - 1) - 1]$ (where indexes 1,2 stand for layers and integer i for lattice site), but since our system is half filled, the expectation value of $\langle \hat{n}_{1,i} \rangle = \langle \hat{n}_{2,i} \rangle = 1$. That is, the charge fluctuations are small. This term can be safely considered as a constant.

Moreover, it is easy to see that $\mathbf{S}_{1i} \cdot \mathbf{S}_{2i}$ and $\hat{Q}_i$ share the same eigenstates and their eigenvalues are different only up to a $1/4$ shift. The eigenstates for $\mathbf{S}_{1i} \cdot \mathbf{S}_{2i}$ and $\hat{Q}_i$ are spin singlet and threefold degenerate spin triplet states,

$$\begin{aligned} |\psi_{0,+0}\rangle &= \frac{1}{\sqrt{2}}(|\uparrow\rangle_1|\downarrow\rangle_2 - |\downarrow\rangle_1|\uparrow\rangle_2), \\ |\psi_{1,+1}\rangle &= (|\uparrow\rangle_1|\uparrow\rangle_2), \\ |\psi_{1,+0}\rangle &= \frac{1}{\sqrt{2}}(|\uparrow\rangle_1|\downarrow\rangle_2 + |\downarrow\rangle_1|\uparrow\rangle_2), \\ |\psi_{1,-1}\rangle &= (|\downarrow\rangle_1|\downarrow\rangle_2). \end{aligned} \quad \text{(A3)}$$

For $\mathbf{S}_{1i} \cdot \mathbf{S}_{2i}$, it is well known that

$$\begin{aligned} \mathbf{S}_{1i} \cdot \mathbf{S}_{2i}|\psi_{0,0}\rangle &= -\tfrac{3}{4}|\psi_{0,0}\rangle, \\ \mathbf{S}_{1i} \cdot \mathbf{S}_{2i}|\psi_{1,m}\rangle &= +\tfrac{1}{4}|\psi_{1,m}\rangle, \quad m = 0,\pm 1. \end{aligned} \quad \text{(A4)}$$

For the $\hat{Q}_i$ interaction, it is simple to show that

$$\begin{aligned} \hat{Q}_i|\psi_{0,0}\rangle &= -1 \cdot |\psi_{0,0}\rangle, \\ \hat{Q}_i|\psi_{1,m}\rangle &= +0 \cdot |\psi_{1,m}\rangle, \quad m = 0,\pm 1. \end{aligned} \quad \text{(A5)}$$

In terms of implementation in the PQMC simulations, for the $\hat{Q}_i$ term, we can directly apply the following Hubbard-Stratonovich transformation to transform the $\hat{Q}_i$ term into the free-fermion system coupled to 4-component Ising fields,

$$\begin{aligned} &\exp\left[-\Delta\tau \frac{J}{8}(D_{1i,2i} - D^{\dagger}_{1i,2i})^2\right] \\ &= \frac{1}{4}\sum_{l=\pm 1,\pm 2} \gamma(l) e^{i\xi_J \eta(l)(D_{1,2} - D^{\dagger}_{1,2})} + \mathcal{O}[(\Delta\tau)^4], \\ &\exp\left[+\Delta\tau \frac{J}{8}(D_{1i,2i} + D^{\dagger}_{1i,2i})^2\right] \\ &= \frac{1}{4}\sum_{l=\pm 1,\pm 2} \gamma(l) e^{\xi_J \eta(l)(D_{1,2} + D^{\dagger}_{1,2})} + \mathcal{O}[(\Delta\tau)^4], \end{aligned} \quad \text{(A6)}$$

with $\xi_J = \sqrt{\Delta\tau J/8}$. For the full $\mathbf{S}_{1i} \cdot \mathbf{S}_{2i}$ interaction term, we need to rewrite it into a summation of the $\hat{Q}_i$ interaction term, the on-site attractive interaction [the second term in Eq. (A7)], and the interlayer density-density attractive interaction [the third term Eq. (A7)] as follows,

$$\begin{aligned} \mathbf{S}_{1i} \cdot \mathbf{S}_{2i} = \hat{Q}_i &- \tfrac{1}{4}[(\hat{n}_{1,i} - 1)^2 + (\hat{n}_{2,i} - 1)^2] \\ &- \tfrac{1}{8}(\hat{n}_{1,i} + \hat{n}_{2,i} - 2)^2. \end{aligned} \quad \text{(A7)}$$

The problem here is that with $J > 0$ (the antiferromagnetic interaction), the simultaneous presence of all these three terms will generate a minus sign problem to the QMC simulation under $U > 0$ condition as the model in Eq. (1), which effectively means that there is no way to perform QMC simulation with the full Heisenberg interaction term for large systems. Although the QMC simulations applying the full J term as Eq. (A7) for the bilayer model under the $U = 0$ condition is free from the sign problem, only keeping the $\hat{Q}_i$ in the $\mathbf{S}_{1i} \cdot \mathbf{S}_{2i}$ interaction during the QMC simulations is still a good approximation, since the single-particle gap is always finite with $U = 0$ and arbitrary J parameter.

APPENDIX B: RAW DATA FOR DYNAMIC CORRELATION FUNCTIONS

In Sec. III B, we present the single-particle as well as the spin excitation gaps at the topological phase transition between QSH and dimer-singlet phases. Here we show some raw data for imaginary-time single-particle Green's function and spin-spin correlation function, to provide the evidence that the extrapolated excitation gaps are in good numerical quality.

Figures 9 and 10 are the raw data of the single-particle Green's function $G(\mathbf{K},\tau)$ and the dynamic spin-spin correlation function $S^{xy}(\mathbf{\Gamma},\tau)$, with parameter set $\lambda = 0.2t, U = 0, J = 3.73t$. According to Fig. 4, this is exactly at $J = J_c$. In Fig. 9(a), we can observe the single-particle gap at the $\mathbf{K}$ point decaying very fast in imaginary time τ. In Fig. 9(b), with a semilogarithmic scale, we can see the size of the single-particle gap almost converging to its thermodynamic limit value for $L = 9,12$ systems. Such fast decay and quick convergence with finite system size actually means the single-particle gap is indeed finite and large at the topological phase transition. In fact it is about $0.7t$ at the transition point.

On the other hand, we can observe that the raw data for the dynamic spin-spin correlation function in Fig. 10(a) decay slower with τ. And in Fig. 10(b) with a semilogarithmic scale, $S^{xy}(\mathbf{\Gamma},\tau)$ shows very good straight lines in imaginary time τ, and we can hence extract the spin gap value with very high accuracy. In fact, the $1/L$ finite-size scaling of the spin

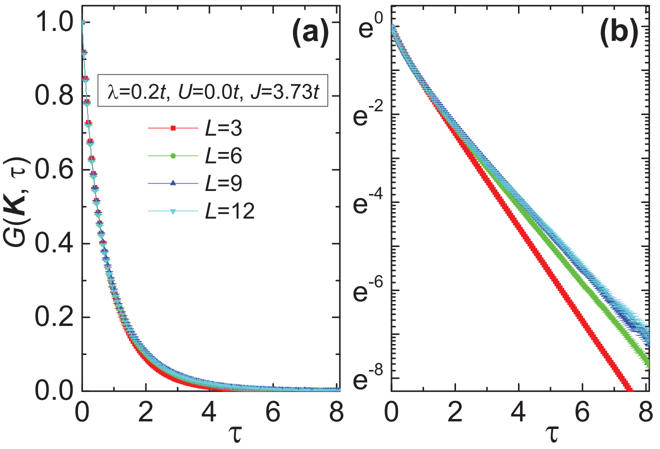

FIG. 9. Single-particle Green's function for $\lambda = 0.2t, U = 0$, $J = 3.73t$ with $L = 3,6,9,12$ at $\mathbf{K}$ point in (a) linear scale and (b) in semilogarithmic scale.

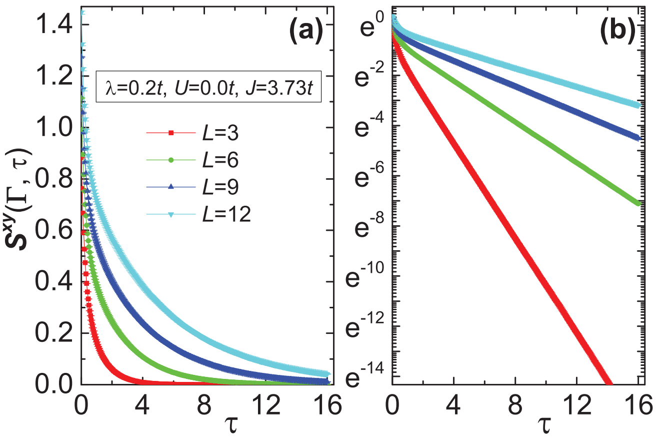

FIG. 10. Dynamic spin-spin correlation function for $\lambda = 0.2t$, $U = 0, J = 3.73t$ with $L = 3,6,9,12$ at $\boldsymbol{\Gamma}$ point in (a) linear scale and (b) in semilogarithmic scale.

gap at $J = 3.73t$ gives rise to a vanishing spin gap in the thermodynamic limit.

APPENDIX C: THE $SO(4)$ SYMMETRY

As mentioned in Sec. II A, the bilayer KMH model given by Eq. (1) has the $U(1)_{\text{spin}} \times [U(1) \times U(1)]_{\text{charge}} \rtimes Z_2^T$ symmetry in general. However when the model parameters are tuned to certain special combinations, the model can have larger symmetries. In this Appendix, we will focus on the various unitary symmetries of the model. The antiunitary time-reversal symmetry Z_2^T is always presented and will be omitted in the following discussion.

To understand the unitary symmetries systematically, let us first introduce three sets of competing orders (in terms of fermion bilinear operators):

$$\begin{aligned} \text{SDW: } \boldsymbol{N}_i &= (-1)^{\xi+i} c_{\xi i}^\dagger \boldsymbol{\sigma} c_{\xi i}, \\ \text{SC: } \Delta_i &= c_{1i}\, i\sigma^y c_{2i}, \\ \text{exciton: } D_i &= (-1)^i c_{1i}^\dagger c_{2i}, \end{aligned} \tag{C1}$$

where $c_{\xi i} = (c_{\xi i\uparrow}, c_{\xi i\downarrow})^\intercal$ is the fermion operator on site i of the ξ layer. $(-1)^\xi$ and $(-1)^i$ respectively denote the staggered sign factors between the layers and between the sublattices. These competing orders anticommute with each other, and can be organized into an $O(7)$ vector: $\boldsymbol{Q}_i = (N_i^x, N_i^y, N_i^z, \operatorname{Re}\Delta_i, \operatorname{Im}\Delta_i, \operatorname{Re}D_i, \operatorname{Im}D_i)$. Then one can introduce the $SO(7)$ group on each site i that rotates the vector $\boldsymbol{Q}_i$. The generators of the $SO(7)$ group are given by the following commutators (for $a < b$ and $a,b = 1,\ldots,7$):

$$\Gamma_i^{ab} = \tfrac{1}{2i}\left[Q_i^a, Q_i^b\right]. \tag{C2}$$

The fermion operator transforms under the $SO(7)$ rotation (parametrized by $\theta_{ab} \in \mathbb{R}$) as

$$c_{\xi i\sigma} \to \exp\left(i\theta_{ab}\Gamma_i^{ab}\right) c_{\xi i\sigma} \exp\left(-i\theta_{ab}\Gamma_i^{ab}\right). \tag{C3}$$

The model Hamiltonian in Eq. (1) cannot achieve this $SO(7)$ symmetry, but its achievable unitary symmetries are all subgroups of this $SO(7)$. Different choices of the model parameters break the $SO(7)$ symmetry differently.

TABLE I. Linearly independent coefficients in C^{ab}. For example, in row N^x, column ReD, the numbers $J - 2U$ and λ mean that the commutation between H and $\frac{1}{2i}[N^x, \operatorname{Re}D]$ contains an operator with coefficient $J - 2U$ and another operator with coefficient λ. The details of the form of the operators are not shown.

		SDW			SC		Exciton	
		N^x	N^y	N^z	ReΔ	ImΔ	ReD	ImD
SDW	N^x		0	λ	U	U	$J-2U, \lambda$	$J-2U, \lambda$
	N^y			λ	U	U	$J-2U, \lambda$	$J-2U, \lambda$
	N^z				U, λ	U, λ	$J-2U$	$J-2U$
SC	Re Δ					0	J, λ	J, λ
	Im Δ						J, λ	J, λ
Exc.	Re D							0
	Im D							

To see how the $SO(7)$ symmetry is broken explicitly by the Hamiltonian, we can calculate the commutator of the Hamiltonian H with the global $SO(7)$ generators $\Gamma^{ab} \equiv \sum_i \Gamma_i^{ab}$:

$$C^{ab} = i[H, \Gamma^{ab}]. \tag{C4}$$

$C^{ab} = 0$ means that the Hamiltonian has the symmetry that rotates Q^a and Q^b. In general, C^{ab} is a linear combination of operators with the model parameters t, λ, U, and J as coefficients:

$$C^{ab} = tC_t^{ab} + \lambda C_\lambda^{ab} + UC_U^{ab} + JC_J^{ab}. \tag{C5}$$

C_t^{ab}, C_λ^{ab}, C_U^{ab}, and C_J^{ab} are complicated operators whose detailed expressions are not of much interest. We only need to extract the coefficients of linearly independent operators, which are concluded in Table I.

Most generally, only 3 (out of 21) $SO(7)$ generators Γ^{12}, Γ^{45}, Γ^{67} commute with the Hamiltonian, as $C^{12} = C^{45} = C^{67} = 0$. They generate the $U(1)_{\text{spin}} \times [U(1) \times U(1)]_{\text{charge}}$ symmetry group. However, when $U = 0$, we have $C^{14} = C^{15} = C^{24} = C^{25} = 0$ in addition, which enlarges the symmetry group to $SO(4) \times U(1)$. The $SO(4)$ symmetry rotates the xy-SDW order and the SC pairing order as an $O(4)$ vector $(N^x, N^y, \operatorname{Re}\Delta, \operatorname{Im}\Delta)$, which involves particle-hole transformations. The $U(1)$ symmetry rotates the exciton order $(\operatorname{Re}D, \operatorname{Im}D)$ and corresponds to the conservation of the charge difference between the layers. When $J = 2U \neq 0$, we have $C^{36} = C^{37} = 0$, which enlarges the symmetry group to $SU(2) \times U(1)_{\text{spin}} \times U(1)_{\text{charge}}$ as mentioned in Ref. [49]. When the interaction is completely turned off as $U = J = 0$, the model has $SO(4) \times SO(3)$ symmetry. On the other hand, in the absence of the spin-orbital coupling, i.e., $\lambda = 0$, the model has even richer symmetry structures, as the spin $SU(2)$ symmetry is restored. Under generic interaction, the symmetry group is $SU(2)_{\text{spin}} \times [U(1) \times U(1)]_{\text{charge}}$, which can be enlarged to $SO(5) \times U(1)$ at $U = 0$, or another $SO(5) \times U(1)$ at $J = 2U$, or $SO(4) \times SU(2)$ at $J = 0$.

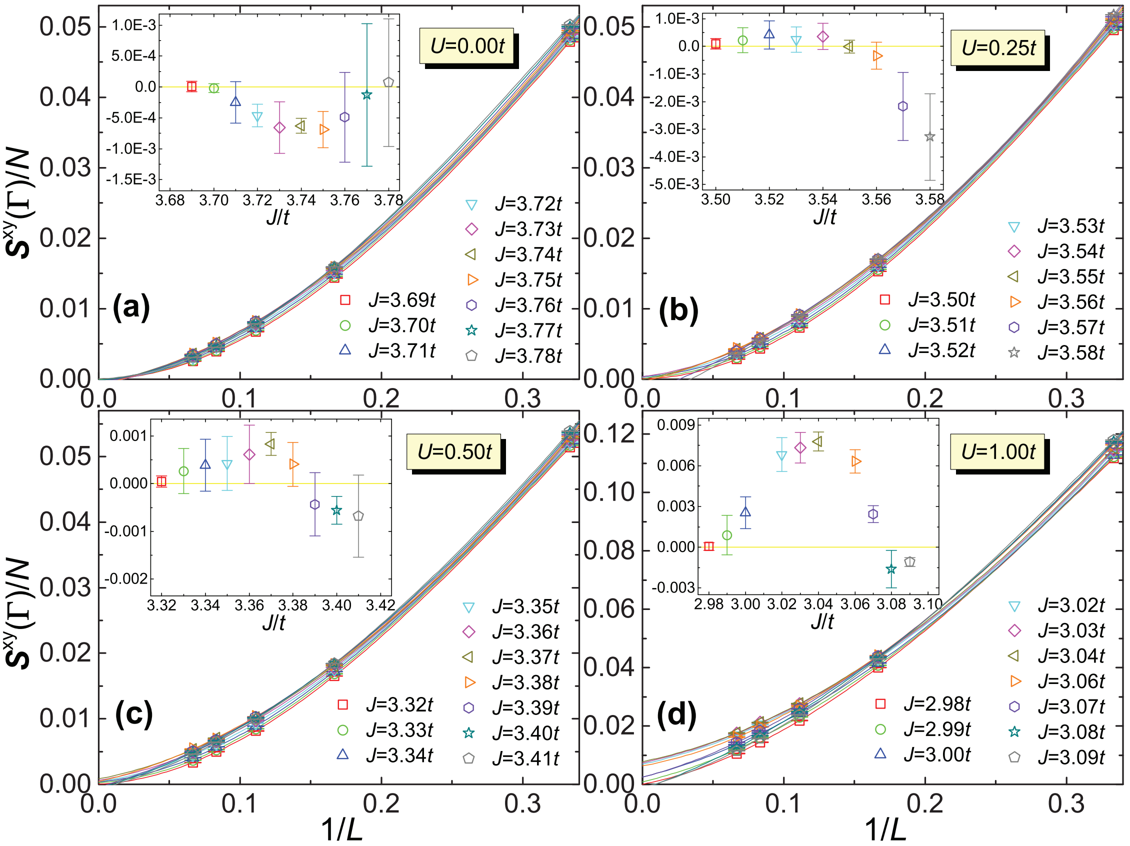

FIG. 11. Extrapolation of structure factor $S^{xy}(\mathbf{\Gamma})/N$ of xy-AFM order over $1/L$ for (a) $U=0$, (b) $U=0.25t$, (c) $U=0.50t$, and (d) $U=1.00t$ over inverse system size $1/L$, at $\lambda=0.2t$. The data points with error bars in the insets are the extrapolated values in the thermodynamic limit.

APPENDIX D: THE TOPOLOGICAL PHASE TRANSITIONS AT SMALL-U REGION

In Sec. III, we present/discuss in detail the results about the J-driven topological phase transition without spontaneous symmetry breaking, including the energy derivatives, excitation gaps, strange correlator, and quantum field theory correspondence. In this part, we show more numerical data about the topological phase transition at the small-U region.

As we have mentioned, the xy-AFM order is absent around the topological phase transition at the small-U region. In Fig. 11, the extrapolation of structure factors of xy-AFM order over $1/L$ for $U=0,0.25t,0.50t,1.0t$ is shown. From the results in Fig. 11, the xy-AFM order is explicitly absent for $U=0$ and $U=0.25$t, corresponding to which the topological phase transition points are $J_c/t=3.73t$ and $J_c/t=3.54t$. For $U=0.5t$, only a single point of $J/t=3.37$ has nonzero xy-AFM order applying the step size $\Delta J=0.01t$ during QMC simulations. Considering the numerical error existing in QMC simulations, it is reasonable to terminate the xy-AFM ordered phase at $U=0.5t$ in the phase diagram presented in Fig. 2. For $U=1.0t$, the extrapolated xy-AFM order [inset of Fig. 11(d)] is nonzero in the $3.00\leqslant J/t\leqslant 3.07$ region, which explicitly demonstrates the stepping in of the xy-AFM ordered phase between the QSH insulator and interlayer dimer-singlet insulator. Based on the results in Figs. 11(a) and 11(b), the topological phase transition without spontaneous symmetry breaking is well established for the $U=0$ and $U=0.25t$ cases, i.e., finite U.

Another question is whether the topological phase transition at small U is of first order or continuous. Due to the fact that there is no nonzero local order parameter across the phase transition, to solve this problem thoroughly is not easy.

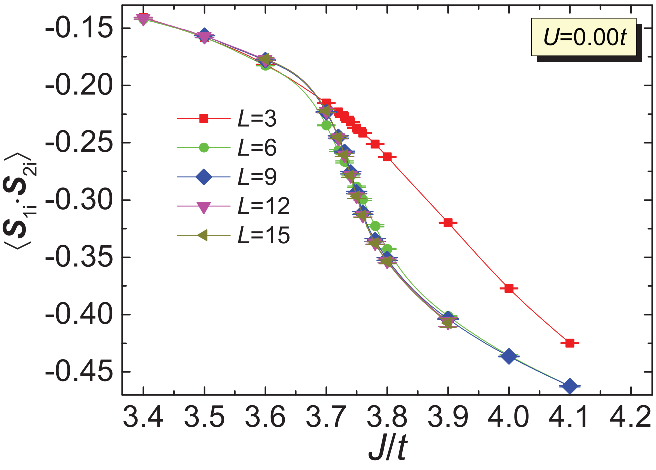

FIG. 12. The interlayer spin-spin correlation functions around the topological phase transitions for $U=0$ with $\lambda=0.2t$.

However, to resolve this problem as best as we can, we have measured the interlayer spin-spin correlation function $\langle \boldsymbol{S}_{1i} \cdot \boldsymbol{S}_{2i} \rangle$ for 5 different system sizes at $U = 0$ as a function of J. As discussed in the main text, this quantity can be taken as the first-order derivative of ground-state energy over the J parameter of the model in Eq. (1). Depending on whether this quantity is continuous or not around the quantum phase transition in the thermodynamic limit, we can determine the order of the transition.

The results of $\langle \boldsymbol{S}_{1i} \cdot \boldsymbol{S}_{2i} \rangle$ for $U = 0$ across the topological phase transition are shown in Fig. 12. We can observe that $\langle \boldsymbol{S}_{1i} \cdot \boldsymbol{S}_{2i} \rangle$ has almost reached the converged values already in the $L = 12$ system, i.e., values at the thermodynamic limit. This is rather reasonable since the fermionic channel of the system is always gapped and the finite-size effect should not be so strong. Most importantly, we indeed observe that $\langle \boldsymbol{S}_{1i} \cdot \boldsymbol{S}_{2i} \rangle$ changes smoothly across the topological phase transition, which suggests a continuous phase transition.

[1] M. Dzero, K. Sun, V. Galitski, and P. Coleman, Phys. Rev. Lett. **104**, 106408 (2010).
[2] J. Jiang, S. Li, T. Zhang, Z. Sun, F. Chen, Z. R. Ye, M. Xu, Q. Q. Ge, S. Y. Tan, X. H. Niu, M. Xia, B. P. Xie, Y. F. Li, X. H. Chen, H. H. Wen, and D. L. Feng, Nat. Commun. **4**, 3010 (2013).
[3] N. Xu, P. K. Biswas, J. H. Dil, R. S. Dhaka, G. Landolt, S. Muff, C. E. Matt, X. Shi, N. C. Plumb, M. Radovic, E. Pomjakushina, K. Conder, A. Amato, S. V. Borisenko, R. Yu, H.-M. Weng, Z. Fang, X. Dai, J. Mesot, H. Ding, and M. Shi, Nat. Commun. **5**, 4566 (2014).
[4] D. A. Pesin and L. Balents, Nat. Phys. **6**, 376 (2010).
[5] J. Maciejko and G. A. Fiete, Nat. Phys. **11**, 385 (2015).
[6] L. Fidkowski and A. Kitaev, Phys. Rev. B **81**, 134509 (2010).
[7] L. Fidkowski and A. Kitaev, Phys. Rev. B **83**, 075103 (2011).
[8] X.-L. Qi, New J. Phys. **15**, 065002 (2013).
[9] H. Yao and S. Ryu, Phys. Rev. B **88**, 064507 (2013).
[10] S. Ryu and S.-C. Zhang, Phys. Rev. B **85**, 245132 (2012).
[11] Z.-C. Gu and M. Levin, Phys. Rev. B **89**, 201113 (2014).
[12] L. Fidkowski, X. Chen, and A. Vishwanath, Phys. Rev. X **3**, 041016 (2013).
[13] C. Wang and T. Senthil, Phys. Rev. B **89**, 195124 (2014).
[14] Y.-Z. You, Y. BenTov, and C. Xu, arXiv:1402.4151.
[15] Y.-Z. You and C. Xu, Phys. Rev. B **90**, 245120 (2014).
[16] Y.-Z. You and C. Xu, Phys. Rev. B **91**, 125147 (2015).
[17] X. Chen, L. Fidkowski, and A. Vishwanath, Phys. Rev. B **89**, 165132 (2014).
[18] P. Bonderson, C. Nayak, and X.-L. Qi, J. Stat. Mech. (2013) P09016.
[19] C. Wang, A. C. Potter, and T. Senthil, Phys. Rev. B **88**, 115137 (2013).
[20] M. A. Metlitski, C. L. Kane, and M. P. A. Fisher, Phys. Rev. B **92**, 125111 (2015).
[21] C. Wang and T. Senthil, Phys. Rev. X **5**, 041031 (2015).
[22] M. A. Metlitski and A. Vishwanath, arXiv:1505.05142.
[23] X. Chen, Z.-C. Gu, Z.-X. Liu, and X.-G. Wen, Phys. Rev. B **87**, 155114 (2013).
[24] X. Chen, Z.-C. Gu, Z.-X. Liu, and X.-G. Wen, Science **338**, 1604 (2012).
[25] S. V. Isakov, Y. B. Kim, and A. Paramekanti, Phys. Rev. Lett. **97**, 207204 (2006).
[26] S. V. Isakov, M. B. Hastings, and R. G. Melko, Nat. Phys. **7**, 772 (2011).
[27] S. V. Isakov, M. B. Hastings, and R. G. Melko, Science **335**, 193 (2012).
[28] T. Grover and A. Vishwanath, Phys. Rev. B **87**, 045129 (2013).
[29] Y.-M. Lu and D.-H. Lee, Phys. Rev. B **89**, 195143 (2014).
[30] Y.-Z. You, Z. Bi, A. Rasmussen, K. Slagle, and C. Xu, Phys. Rev. Lett. **112**, 247202 (2014).
[31] H.-Q. Wu, Y.-Y. He, Y.-Z. You, C. Xu, Z. Y. Meng, and Z.-Y. Lu, Phys. Rev. B **92**, 165123 (2015).
[32] K. Wierschem and P. Sengupta, Phys. Rev. Lett. **112**, 247203 (2014).
[33] K. Wierschem and P. Sengupta, Phys. Rev. B **90**, 115157 (2014).
[34] T. Scaffidi and Z. Ringel, Phys. Rev. B **93**, 115105 (2016).
[35] C. L. Kane and E. J. Mele, Phys. Rev. Lett. **95**, 146802 (2005).
[36] C. L. Kane and E. J. Mele, Phys. Rev. Lett. **95**, 226801 (2005).
[37] S. Rachel and K. Le Hur, Phys. Rev. B **82**, 075106 (2010).
[38] S.-L. Yu, X. C. Xie, and J.-X. Li, Phys. Rev. Lett. **107**, 010401 (2011).
[39] W. Wu, S. Rachel, W.-M. Liu, and K. Le Hur, Phys. Rev. B **85**, 205102 (2012).
[40] Y.-H. Chen, H.-H. Hung, G. Su, G. A. Fiete, and C. S. Ting, Phys. Rev. B **91**, 045122 (2015).
[41] M. Hohenadler, T. C. Lang, and F. F. Assaad, Phys. Rev. Lett. **106**, 100403 (2011).
[42] D. Zheng, G.-M. Zhang, and C. Wu, Phys. Rev. B **84**, 205121 (2011).
[43] M. Hohenadler, Z. Y. Meng, T. C. Lang, S. Wessel, A. Muramatsu, and F. F. Assaad, Phys. Rev. B **85**, 115132 (2012).
[44] F. F. Assaad, M. Bercx, and M. Hohenadler, Phys. Rev. X **3**, 011015 (2013).
[45] H.-H. Hung, L. Wang, Z.-C. Gu, and G. A. Fiete, Phys. Rev. B **87**, 121113 (2013).
[46] T. C. Lang, A. M. Essin, V. Gurarie, and S. Wessel, Phys. Rev. B **87**, 205101 (2013).
[47] H.-H. Hung, V. Chua, L. Wang, and G. A. Fiete, Phys. Rev. B **89**, 235104 (2014).
[48] Z. Y. Meng, H.-H. Hung, and T. C. Lang, Mod. Phys. Lett. B **28**, 1430001 (2014).
[49] K. Slagle, Y.-Z. You, and C. Xu, Phys. Rev. B **91**, 115121 (2015).
[50] F. Assaad and H. Evertz, in *Computational Many-Particle Physics*, edited by H. Fehske, R. Schneider, and A. Weiße, Lecture Notes in Physics Vol. 739 (Springer, Berlin, 2008), pp. 277–356.
[51] F. F. Assaad, Phys. Rev. B **71**, 075103 (2005).
[52] Z. Y. Meng, T. C. Lang, S. Wessel, F. F. Assaad, and A. Muramatsu, Nature (London) **464**, 847 (2010).
[53] It is well known that most topological insulators can be described by Dirac fermions at low energy, and the bosonic SPT states can be described by either a nonlinear sigma model field theory [59] or a Chern-Simons field theory [65], both of which have an effective Lorentz invariance.

[54] M. Laubach, J. Reuther, R. Thomale, and S. Rachel, Phys. Rev. B **90**, 165136 (2014).

[55] F. Grandi, F. Manghi, O. Corradini, and C. M. Bertoni, Phys. Rev. B **91**, 115112 (2015).

[56] T. Yoshida, R. Peters, S. Fujimoto, and N. Kawakami, Phys. Rev. Lett. **112**, 196404 (2014).

[57] Y.-Z. You, Z. Bi, A. Rasmussen, M. Cheng, and C. Xu, New J. Phys. **17**, 075010 (2015).

[58] C. Xu and T. Senthil, Phys. Rev. B **87**, 174412 (2013).

[59] Z. Bi, A. Rasmussen, K. Slagle, and C. Xu, Phys. Rev. B **91**, 134404 (2015).

[60] H. Levine, S. B. Libby, and A. M. M. Pruisken, Phys. Rev. Lett. **51**, 1915 (1983).

[61] H. Levine, S. B. Libby, and A. M. M. Pruisken, Nucl. Phys. B **240**, 30 (1984); **240**, 49 (1984); **240**, 71 (1984).

[62] A. M. M. Pruisken, M. A. Baranov, and M. Voropaev, arXiv:cond-mat/0101003.

[63] C. Xu and A. W. W. Ludwig, Phys. Rev. Lett. **110**, 200405 (2013).

[64] Y.-Z. You, Z. Bi, D. Mao, and C. Xu, Phys. Rev. B **93**, 125101 (2016).

[65] Y.-M. Lu and A. Vishwanath, Phys. Rev. B **86**, 125119 (2012).